Research Article

Nano Research
2022, 15(1): 186–194

ISSN 1998-0124 CN 11-5974/O4
https://doi.org/10.1007/s12274-021-3455-3

Improving the intrinsic electronic conductivity of $NiMoO_4$ anodes by phosphorous doping for high lithium storage

Luchao Yue[1,2], Chaoqun Ma[3], Shihai Yan[3], Zhenguo Wu[1], Wenxi Zhao[2], Qian Liu[2] (✉), Yonglan Luo[2], Benhe Zhong[1], Fang Zhang[4], Yang Liu[5], Abdulmohsen Ali Alshehri[6], Khalid Ahmed Alzahrani[6], Xiaodong Guo[1] (✉), and Xuping Sun[2] (✉)

[1] *School of Chemical Engineering, Sichuan University, Chengdu 610065, China*
[2] *Institute of Fundamental and Frontier Sciences, University of Electronic Science and Technology of China, Chengdu 610054, China*
[3] *College of Chemistry and Pharmaceutical Sciences, Qingdao Agricultural University, Qingdao 266109, China*
[4] *National Engineering Research Center for Nanotechnology, No. 28 East Jiang Chuan Road, Shanghai 200241, China*
[5] *School of Materials Science and Engineering, Henan Normal University, Xinxiang 453007, China*
[6] *Chemistry Department, Faculty of Science, King Abdulaziz University, P.O. Box 80203, Jeddah 21589, Saudi Arabia*

Received: 6 February 2021 / **Revised:** 13 March 2021 / **Accepted:** 15 March 2021

ABSTRACT

Heteroatom doping is one of the most promising strategies toward regulating intrinsically sluggish electronic conductivity and kinetic reaction of transition metal oxides for enhancing their lithium storage. Herein, we designed phosphorus-doped $NiMoO_4$ nanorods (P-$NiMoO_4$) by using a facile hydrothermal method and subsequent low-temperature phosphorization treatment. Phosphorus doping played an indispensable role in significantly improving electronic conductivity and the Li^+ diffusion kinetics of $NiMoO_4$ materials. Experimental investigation and density functional theory calculation demonstrated that phosphorus doping can expand the interplanar spacing and alter electronic structures of $NiMoO_4$ nanorods. Meanwhile, the introduced phosphorus dopant can generate some oxygen vacancies on the surface of $NiMoO_4$, which can accelerate Li^+ diffusion kinetics and provide more active site for lithium storage. As excepted, P-$NiMoO_4$ electrode delivered a high specific capacity (1,130 $mAh \cdot g^{-1}$ at 100 $mA \cdot g^{-1}$ after 100 cycles), outstanding cycling durability (945 $mAh \cdot g^{-1}$ at 500 $mA \cdot g^{-1}$ over 200 cycles), and impressive rate performance (640 $mAh \cdot g^{-1}$ at 2,000 $mA \cdot g^{-1}$) for lithium ion batteries (LIBs). This work could provide a potential strategy for improving intrinsic conductivity of transition metal oxides as high-performance anodes for LIBs.

KEYWORDS

$NiMoO_4$, phosphorus doping, anode, lithium ion batteries

1 Introduction

The ever-increasing demands for portable electronic devices and electrical vehicles look toward the pursuit of lithium ion batteries (LIBs) with high energy and power densities, as well as ultralong lifespan [1–4]. It is widely recognized that striving for a promising anode material is the key point to achieve the above expectations. Among the multitude of alternatives, transition metal oxide, in particularly $NiMoO_4$, has gradually aroused attention as an alluring anode for LIBs owing to its multiple accessible valence states, noteworthy high theoretical capacity, and relatively low cost [5–7]. Analogous to other transition metal oxides, $NiMoO_4$ goes through poor electronic conductivity, sluggish reaction kinetics, and substantial volume expansion, resulting in inferior rate capability and unsatisfactory cycling stability. To reconcile these issues, various strategies such as devising nanostructure and coupling with carbonaceous materials have emerged and developed [8–12]. Generally, designing diverse nanostructured materials can shorten Li^+ diffusion length, but the insufficient electronic conductivity is still desired to conquer. Hybridization with carbonaceous materials can modify the electronic conductivity, however, the decrease in specific capacity of the whole electrode will be occurring [7, 13, 14]. This has led to intense research activities driving to develop doping strategies in an effort to enhance the intrinsic electronic conductivity of $NiMoO_4$ electrode.

Currently, a wealth of literature has demonstrated that heteroatom doping is considered to be the most direct way of improving the electronic conductivity of transition metal oxides by altering the electronic structure [15, 16]. This is because metallic dopants served as electron donors or nonmetal dopants as electron acceptor could redistribute the charge around doping sites and generate impurity bands inside the bandgaps, significantly enhancing the electronic conductivity of transition metal oxides [17–21]. For example, Song et al. [22] doped Mo^{6+} into $TiNb_2O_7$ to improve electronic conductivity of Nb_2O_5, which was because that Mo^{6+} with a higher valence than Ti^{4+} and Nb^{5+} could enhance electron densities near Ti, and Nb by compensating charge into doping site. In addition, Mo doping also facilitated Li^+ diffusion in the lattice via increasing electron density near O and thus achieving an impressive rate capability in LIBs. Besides, Yan et al. [21] fabricated carbon-doped Co_3O_4 nanotubes using polymeric nanofibers as the template, which delivered superior rate and cycling

Address correspondence to Qian Liu, liuqian@uestc.edu.cn; Xiaodong Guo, xiaodong2009@scu.edu.cn; Xuping Sun, xpsun@uestc.edu.cn.

performances. Such excellent lithium storage capability mainly originated from the introduced carbon dopants, which are reflected in three aspects: (i) improving the electronic conductivity; (ii) inducing oxygen vacancies and extending lattices; (iii) generating more active Co^{2+} cations.

Phosphorus possesses lone-pair electrons in 3p orbitals and vacant 3d orbitals, which can tempt local charge density and modulated electronic structure of transition metal oxides. This makes it an astute choice as a dopant to metals oxides and thus is expected to modify the electronic conductivity of transition metal oxides as well [23, 24]. Moreover, phosphorus has been indicated as a fascinating candidate owing to its abundant resource and extraordinarily high theoretical capacity (2,596 $mAh·g^{-1}$, storing three Li atoms forming Li_3P) for LIBs [8, 10]. Benefiting from these merits of phosphorus, P-doped $NiMoO_4$ materials have been reported and characterized in electrochemical catalysts fields, yet never used as anode materials for LIBs. Consequently, one can envisage that phosphorus doping $NiMoO_4$ can enlarge the lithium storage capacity of $NiMoO_4$.

In this light, we demonstrated phosphorus-doped $NiMoO_4$ nanorods (henceforth, P-$NiMoO_4$) as a fascinating anode material for LIBs. P-$NiMoO_4$ nanorods were facilely derived from $NiMoO_4$ precursors via low-temperature annealing adopting NaH_2PO_2 as the phosphorus source. The density functional theory (DFT) calculations explained substitution of O with P would decrease the bandgap of $NiMoO_4$, leading to the improvement in electronic conductivity. Meanwhile, some oxygen vacancies were generated under the phosphorization process, further increasing more active sites for lithium storage. In addition, one-dimensional nanostructured $NiMoO_4$ with a high length-to-diameter ratio could shorten Li^+ diffusion length and tolerated relaxed mechanical strain upon lithium storage process. Benefiting from these merits, the as-prepared P-$NiMoO_4$ nanorods exhibit superior capacity and high-rate performance compared with undoped $NiMoO_4$ nanorods.

2 Experimental

2.1 Preparation of P-$NiMoO_4$

P-$NiMoO_4$ nanorods were synthesized through the simple hydrothermal method, calcination treatment, and subsequent phosphorization processes. Here, 1.5 mmol $Ni(NO_3)_2$ and 1.5 mmol Na_2MoO_4 were dissolved into 60 mL deionized (DI) water under constant magnetic stirring. The obtained light green solution was transferred into a 100 mL Teflon-lined stainless steel autoclave and maintained at 150 °C for 5 h in an oven. After cooled down naturally, the green product was washed several times with DI water and alcohol to remove impurities. Then the product was converted to $NiMoO_4$ through annealing at 500 °C for 2 h in the air. Lastly, two ceramic boats containing $NiMoO_4$ and NaH_2PO_2 were placed in the downstream and upstream of the tubular furnace respectively. Under Ar atmosphere, the samples were heated to 300 °C for 1 h with a heating rate of 2 $°C·min^{-1}$.

2.2 Characterization

The crystalline structures of the as-prepared samples were analyzed by X-ray diffraction (XRD, DX-2700BH). High-temperature XRD (H-XRD) measured by a Philips PW1730 diffractometer was conducted in the air using an *in-situ* temperature-programmed heating mode. Scanning electron microscopy (SEM) and corresponding energy-dispersive X-ray (EDX) mapping images were collected on Gemini SEM 300 field emission scanning electron microscopy. Transmission electron microscopy (TEM) and high-resolution TEM (HRTEM) images were obtained by FEI TF20 electron microscopy. The valence states of materials were investigated by the X-ray photoelectron spectroscopy (XPS, ESCALABMK II) using Mg as the exciting source. EPR experiments were conducted by a Bruker ELEXSYS E580 spectrometer.

2.3 Electrochemical measurements

The electrochemical performances were evaluated in CR2025 half cells which were assembled in a glove box in an argon atmosphere. The working electrodes were prepared by coating the slurry active materials ($NiMoO_4$ and P-$NiMoO_4$), Ketjen Black, and polyvinylidene fluoride (PVDF) with a mass ratio of 70:20:10 using N-Methyl pyrrolidone as the solvent on Cu foil. After drying at 100 °C under vacuum overnight, the electrode was pressed and cut into disks. The mass loading of the active materials is 1.5–2.0 mg for a single electrode. Li foil was utilized as counter electrode, and Celgard 2400 film was served as separator, while the electrolyte contained 1 M $LiPF_6$ dissolved in a mixture of ethylene carbonate (EC), diethyl carbonate (DEC), and 5 wt.% of fluoroethylene carbonate (FEC). The galvanostatic charge/discharge cycling was carried out on a Neware battery tester (Shenzhen, Xinwei) in a voltage window from 0.01 to 3.0 V. GITT was carried out on a LAND battery measurement apparatus (CT3001A) to calculate the Li^+ diffusion coefficient. CV and EIS tests were conducted on a CHI 660E electrochemical workstation (Chenhua, Shanghai).

2.4 Computational method

The calculations were carried out utilizing the Vienna Ab Initio Simulation Package (VASP) [25, 26]. The projected enhancement wave pseudopotential [27] and the Perdew-Burke-Ernzerhof (PBE) function [28] based on the generalized gradient approximation were performed to optimize the structure and calculate the exchange and correlation energies until the total energy on all atoms and force were converged to 10^{-5} eV/atom and 0.05 $eV·Å^{-1}$, respectively. The cut-off energy of plane-wave basis set was 500 eV and Brillouin region on the grid with a 20 × 20 × 20 and 7 × 7 × 7 *k*-point was performed for calculation of bandgap and density of states, respectively. A vacuum region of 10 $Å^{-1}$ was built in the model of $NiMoO_4$ and P-$NiMoO_4$, and van der Waals interactions corrected using DFT-D_2 are considered [29].

3 Results and discussion

The designed concept of heteroatom doping is to introduce a suitable species into $NiMoO_4$ materials, aiming to improve electronic conductivity and reaction kinetics in the electrode. The driving force is undoubtedly originated from the reduced bandgap and generated impurity bands inside the bandgaps [17, 30]. In this work, phosphorous atoms were purposely chosen to enhance the electronic conductivity of $NiMoO_4$, and the corresponding synthesis process was expounded in Fig. 1(a). First of all, a facile approach of hydrothermal treatment was used to synthesize the precursor (hydrated $NiMoO_4$ nanorods). Then, the precursors were calcined in the muffle roaster to fabricate $NiMoO_4$ nanorods, in which the calcination temperature was confirmed by *in-situ* H-XRD in a temperature range of 15–600 °C (Fig. 1(b)). As shown in Fig. 1(c), the resulting samples produced via hydrothermal treatments display the hydrated $NiMoO_4$ phase which is stable up to 480 °C. When the temperature is increased to 500 °C, the diffraction peaks of the hydrated $NiMoO_4$ phase have disappeared accompanied by the emergence of the $NiMoO_4$ phase. It is noted that the crystallinity increases with the ascent in temperature but the diffraction peaks appear with less intensity when the temperature is further elevated to 600 °C. Based on the above analysis, the high crystalline

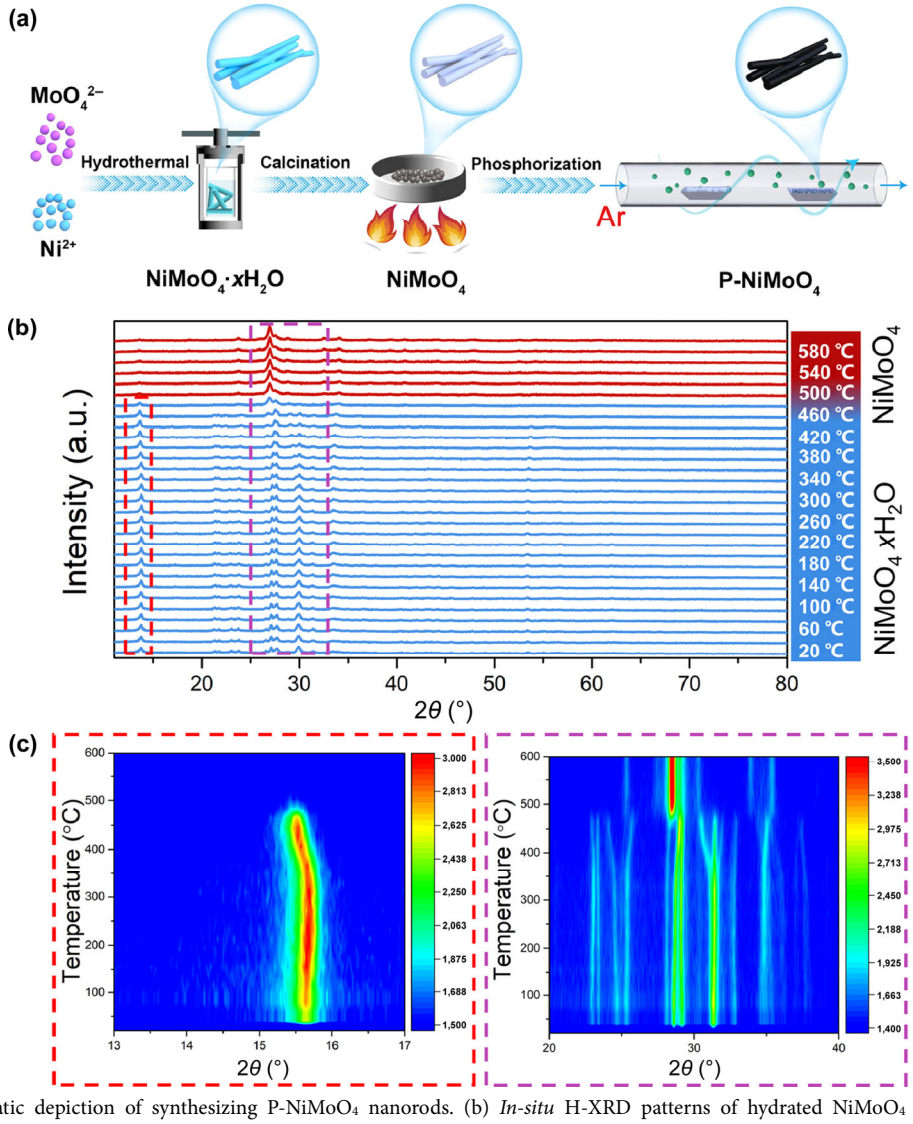

Figure 1 (a) Schematic depiction of synthesizing P-$NiMoO_4$ nanorods. (b) *In-situ* H-XRD patterns of hydrated $NiMoO_4$ precursors and (c) the corresponding contour plots in *in-situ* XRD for the selected 2θ range.

$NiMoO_4$ phase can be obtained by calcinating under the air at ~ 500 °C. Ultimately, P-$NiMoO_4$ nanorods were fabricated by low-temperature phosphorization treatment.

The morphologies and structures of $NiMoO_4$ and P-$NiMoO_4$ nanorods were characterized by SEM and TEM techniques. It is clearly seen that $NiMoO_4$ consists of nanorods with several micrometers in length and the average diameter around 300 nm (Figs. 2(a) and 2(b)). Notably, the nanorod feature is well-preserved after P-doping (Figs. 2(d) and 2(e)). Such 1D nanorod architecture of P-$NiMoO_4$ with a high length-diameter ratio benefits lithium storage since it possesses bifunctional features that facilitate electronic and ionic transport as well as offer strong tolerance to stress-strain upon charge/discharge process [14, 31, 32]. As shown in the HRTEM image (Fig. 2(c)), the interplanar distance of 0.300 nm is assigned to the (220) plane of $NiMoO_4$, which is well matched with the XRD results. Note that the corresponding lattice fringe spacing of the (220) plane in P-$NiMoO_4$ is 0.305 nm (Fig. 2(f)), which is slightly larger than that of undoped $NiMoO_4$ due to P doping into the lattice of $NiMoO_4$, which can accelerate the lithium-ion diffusion in the lattice [5, 33]. Furthermore, the diffraction spots from SAED pattern (Fig. S1 in the ESM) confirms that the enlarge of lattice spacing in P-$NiMoO_4$ materials, and the single crystalline nature of $NiMoO_4$ still remains after introducing P. Besides, the elemental mapping images of P-$NiMoO_4$ (Fig. 2(g)) further

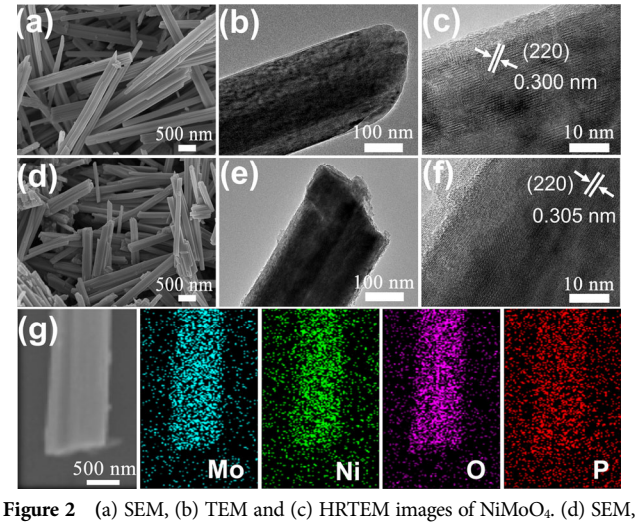

Figure 2 (a) SEM, (b) TEM and (c) HRTEM images of $NiMoO_4$. (d) SEM, (e) TEM, and (f) HRTEM images of P-$NiMoO_4$. (g) EDX mapping images of P-$NiMoO_4$.

confirm the uniform distribution of Ni, Mo, O, and P elements in the nanorod.

The crystalline evolution of $NiMoO_4$ materials after introducing phosphorus was investigated via XRD. The Rietveld refinement

plots of XRD patterns (Fig. 3(a)) revealed that both $NiMoO_4$ and P-$NiMoO_4$ show similar crystalline structures and all the diffraction peaks correspond to monoclinic $NiMoO_4$ phase (JCPDS 86-0631), demonstrating that the crystalline phase of $NiMoO_4$ does not significantly change by P doping without the existence of crystallized nickel/molybdenum phosphates or phosphides. Compared with undoped $NiMoO_4$, P-$NiMoO_4$ exhibits narrower half-peak width and better intensity, which may be attributed to the phosphorization treatment under 300 °C. Of particular note is that a marginally negative shift of the diffraction peaks is identified after P doping. For example, the (220) diffraction peak at 28.9° in P-$NiMoO_4$ slightly shifts to a smaller angle value (Fig. 3(b)), suggesting that phosphorus atoms are incorporated into the lattices of $NiMoO_4$ and causing slight lattice deformation, which is in agreement with the HRTEM results. To further confirm the crystalline structure change produced by P doping, the unit cell parameters are acquired through refining the XRD patterns of both samples, and corresponding calculated result is presented in Table S1 in the ESM. With P doping, the unit cell volume of $NiMoO_4$ slightly extend from 294.77 to 295.62 $Å^3$, which is ascribed to the substitution of O by larger P.

The valence state and chemical composition of as-prepared samples were analyzed by XPS. The full survey spectra of $NiMoO_4$ materials indicate the presence of Ni, Mo and O elements, while an additional peak of P is detected in P-$NiMoO_4$ (Fig. S2 in the ESM). As expounded in Fig. 3(c), the high-resolution Ni 2p signal of $NiMoO_4$ and P-$NiMoO_4$ can be divided into four peaks. The deconvolved shoulder peaks at binding energies of 855.3 and 861.4 eV indexed to Ni $2p_{3/2}$ and its satellite peak; another two peaks observed at 872.6 and 879.3 eV are the characteristic of Ni $2p_{1/2}$ and its satellite peaks. It demonstrates the existence of Ni^{2+} in $NiMoO_4$ and P-$NiMoO_4$ [34–36]. In contrast to the spectra of $NiMoO_4$, a marginally negative shift of Ni $2p_{3/2}$ in P-$NiMoO_4$ indicates the generation of Ni^{x+} species ($0 < x < 2$) [5]. For Mo 3d spectra (Fig. 3(d)), two main peaks located at 231.7 and 234.9 eV are associated with the feature of Mo^{6+} $3d_{5/2}$ and $3d_{3/2}$ peaks, respectively [37]. However, except for Mo^{6+}, Mo^{5+} $3d_{5/2}$ and $3d_{3/2}$ peaks emerged at 230.8 and 233.9 eV are attributed to the partial reduction of Mo^{6+} during the phosphorization treatment process [38]. The peaks of P $2p_{1/2}$ (129.9 eV) and P $2p_{3/2}$ (128.8 eV) can be observed in the high- resolution P 2p spectra (Fig. 3(e)), associating with the combination of P and metals (Ni and Mo) in P-$NiMoO_4$. Another peak located at 133.8 eV is indexed to P-O band produced by inevitable air contact [34, 39, 40]. The O 1s signals for $NiMoO_4$ (Fig. 3(f)) is also divided into the doublet peaks at 529.8 (O I) and 531.6 eV (O II), assigning to the lattice oxygen atoms and surface oxygen, respectively. In particular, O peaks shift to higher energy state for P-$NiMoO_4$ and the proportion of O II peaks increases after introducing P, which may be attributed to the existence of oxygen vacancies [41, 42]. Furthermore, the obviously characteristic EPR signal (Fig. S3 in the ESM) also declares the existence of oxygen vacancies in P-$NiMoO_4$, which can boost the lithium storage capacity to some content.

The lithium storage behaviors of resultant samples were estimated in a typical coin-type cell. Figure 4(a) and Fig. S4(a) in the ESM presented the initial three cyclic voltammetry (CV) profiles of $NiMoO_4$ and P-$NiMoO_4$ nanorods at 0.5 $mV·s^{-1}$ in a potential range of 0.01–3.0 V. During the first cathodic scan, a wide reduction peak located at 1.14 V is associated with the formation of solid electrolyte interphase (SEI) film at the electrode/electrolyte interface [12, 13]. The following cathodic peak at 0.39 V might correspond to insertion of Li^+ into the lattice of P-$NiMoO_4$ and subsequent reduction of P-$NiMoO_4$ to metallic Ni and Mo. In the reverse process, two peaks appearing at around 1.53 and 2.3 V are associated with the oxidation reaction of Ni to $Ni^{2+}$and Mo to Mo^{6+} accompanying the decomposition of Li_2O, respectively [43, 44]. Notably, two reduction peaks at 0.62 and 1.60 V are observed in subsequent CV curves, which stands for the reversible reductive reaction of MoO_3 and NiO to Mo and Ni metals, respectively [45–47]. Furthermore, the position of reduction and oxidation peaks in the following cycles overlap very well, which demonstrates the excellent reversibility and stability of P-$NiMoO_4$ electrode during the lithium storage process.

The lithium storage capacities of as-synthesized samples were further evaluated through galvanostatic discharge/charge measurement. As illustrated in Fig. 4(b), P-$NiMoO_4$ electrode gives the initial discharge and charge capacities of 1,645 and 958 $mAh·g^{-1}$ at 100 $mA·g^{-1}$, respectively, and corresponding to an initial Coulombic efficiency of 58%. In terms of undoped $NiMoO_4$ electrode, the first discharge and charge capacities are around 1,556 and 814 $mAh·g^{-1}$ at 100 $mA·g^{-1}$ (Fig. S4(b) in the ESM). This irreversible capacity loss in the first cycles could be ascribed to the formation of SEI film on the electrode surface [48]. Besides, P-$NiMoO_4$ electrode achieves the specific capacity of 1,130 $mAh·g^{-1}$ over 100 cycles at 100 $mA·g^{-1}$, which is superior

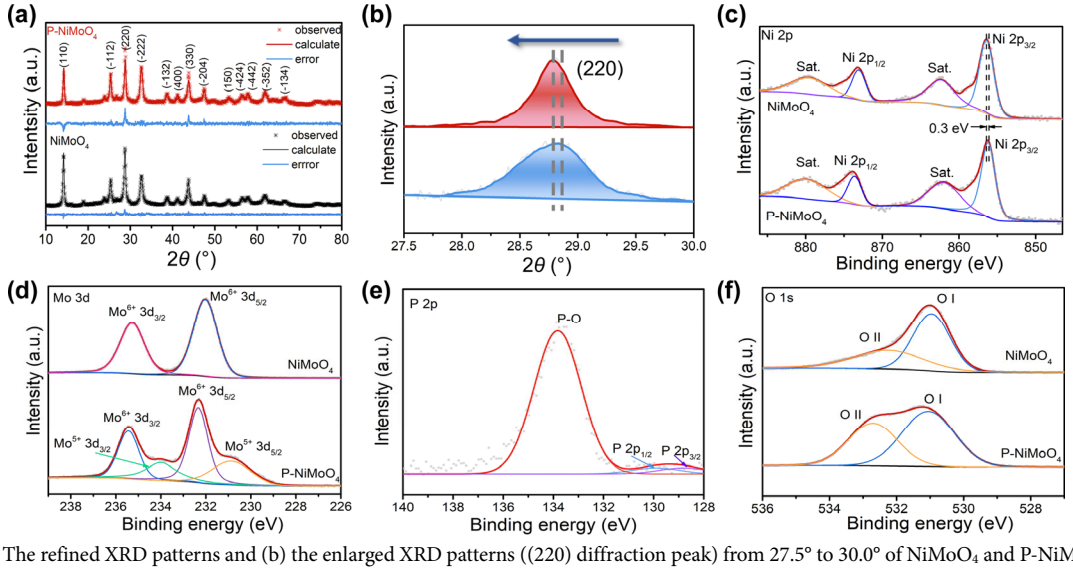

Figure 3 (a) The refined XRD patterns and (b) the enlarged XRD patterns ((220) diffraction peak) from 27.5° to 30.0° of $NiMoO_4$ and P-$NiMoO_4$. (c) Ni 2p and (d) Mo 3d XPS spectra of $NiMoO_4$ and P-$NiMoO_4$. (e) P 2p XPS spectra of P-$NiMoO_4$. (f) O 1s XPS spectra of $NiMoO_4$ and P-$NiMoO_4$.

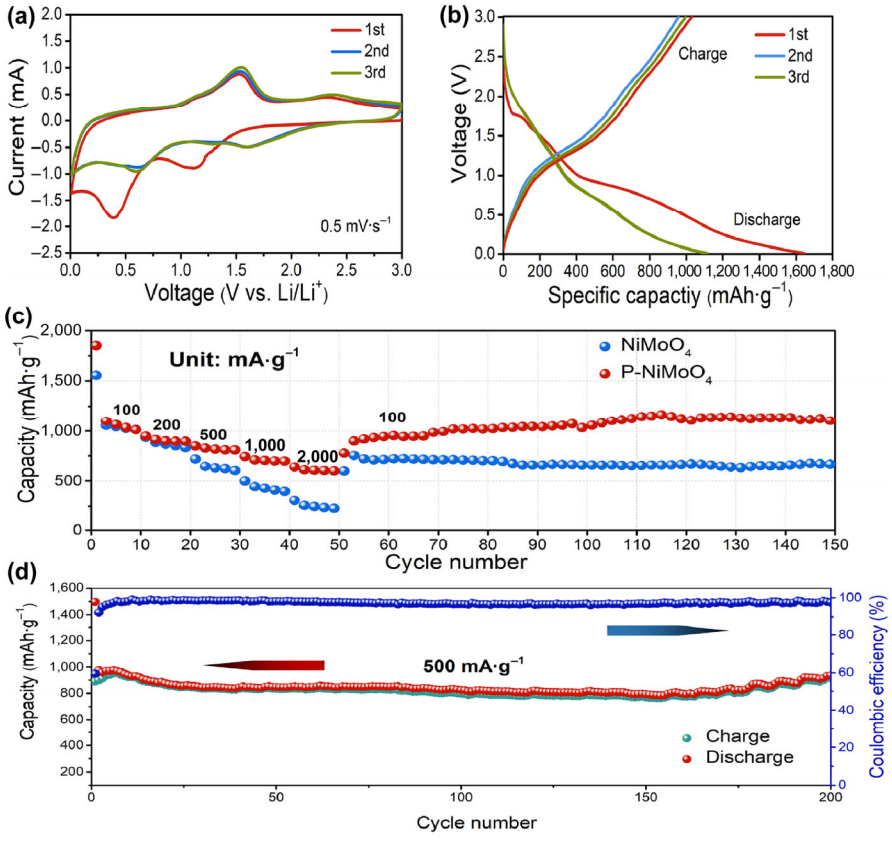

Figure 4 (a) CV curves of P-$NiMoO_4$ electrode at 0.5 mV·s^{-1}. (b) Galvanostatic discharge-charge curves of P-$NiMoO_4$ electrode at 100 mA·g^{-1}. (c) Rate capabilities of $NiMoO_4$ and P-$NiMoO_4$ electrodes. (d) Long-term cycling performance of P-$NiMoO_4$ electrode.

than that of the undoped $NiMoO_4$ electrode in a control experiment (594 mAh·g^{-1}) (Fig. S5 in the ESM). The overall morphology of P-$NiMoO_4$ nanorods is retained after long term cycling, as presented in Figs. S6 and S7 in the ESM. Such enhanced lithium storage capability of P-$NiMoO_4$ electrode is possibly attributed to P doping, which can generate oxygen vacancies and provide more active sites to store Li^+.

The rate capacities of $NiMoO_4$ and P-$NiMoO_4$ electrodes are represented in Fig. 4(c), where the current density is progressively elevated from 100 to 2,000 mA·g^{-1} for every 10 consecutive cycles and subsequently recovering to 100 mA·g^{-1} for 100 cycles. As one can see that P-$NiMoO_4$ electrode can sustain higher specific capacity than undoped $NiMoO_4$ electrode under different rate, especially at high current density. Indeed, the P-$NiMoO_4$ electrode delivered a high reversible capacity of 807 mAh·g^{-1} at 1,000 mA·g^{-1}. Even increased to 2,000 mA·g^{-1}, a fascinating capacity of 640 mAh·g^{-1} can be achieved, exhibiting two times improvement than that of undoped $NiMoO_4$ electrode (305 mAh·g^{-1}). Moreover, the capacity around 1,116 mAh·g^{-1} can be realized after 100 cycles when the current density returns to 100 mA·g^{-1}, manifesting an excellent rate capability of P-$NiMoO_4$ electrode. The significantly enhanced rate capacity accompanied by exceptional cycling performance should be closely related to P doping, which can modify the electronic conductivity and generate some oxygen vacancies on the surface of $NiMoO_4$. In comparison with previous reported $NiMoO_4$ based materials, like $NiMoO_4$@C nanowire (580 mAh·g^{-1} at 2,000 mA·g^{-1}) [6], $NiMoO_4$ ultrathin nanosheets (600 mAh·g^{-1} at 2,000 mA·g^{-1}) [13], $NiMoO_4$-CNFs composite (556.2 mAh·g^{-1} at 2,000 mA·g^{-1}) [14], this work manifests significantly superiority in the improvement of electronic conductivity of $NiMoO_4$ materials by P doping. Meanwhile, the electrochemical performances of other P-doped hybrid anode materials for LIBs are also listed in Table S2 in the ESM, which indicate the phosphorus doping is promising strategy to improve their lithium storage capacity. Furthermore, the long-term cycling durability of P-$NiMoO_4$ electrode is evaluated at 500 mA·g^{-1}. As shown in Fig. 4(d), P-$NiMoO_4$ electrode have a promising reversible capacity of 945 mAh·g^{-1} with a Coulombic efficiency approaching 100% even after 200 cycles, demonstrating an outstanding cycling durability of P-$NiMoO_4$ electrode.

Such improved lithium storage capacity of P-$NiMoO_4$ electrode should benefit from P doping, which is further demonstrated by electrochemical impedance spectra (EIS) results. The EIS patterns of P-$NiMoO_4$ and $NiMoO_4$ electrodes are recorded after scanning for three cycles at 0.5 mV·s^{-1}, as illustrated in Fig. 5(a). Two semicircles in high-frequency and high-medium-frequency regions should be assigned to resistances of SEI film (R_f) and charge-transfer (R_{ct}), respectively [49, 50]. In light of the equivalent circuit (inset of Fig. 5(a)), it can be calculated that R_{ct} value of P-$NiMoO_4$ electrode (46.22 Ω) is smaller than that of undoped $NiMoO_4$ electrode (80.06 Ω), indicating a faster charge transfer at the interface. In addition, the R_f value of P-$NiMoO_4$ electrode (2.51 Ω) is also smaller than that of undoped $NiMoO_4$ electrode (3.19 Ω), which demonstrates that P doping may repress the overgrowth of SEI film at the electrode/electrolyte interfaces. The declined resistance of P-$NiMoO_4$ electrode also explained by the improvement of electronic conductivity and the extended lattice after P doping [51, 52]. Additionally, to understand the diffusion kinetic behavior of $NiMoO_4$ and P-$NiMoO_4$ electrodes, the galvanostatic intermittent titration technique (GITT) is carried out with a pulse current density of 200 mA·g^{-1} (Fig. 5(b)). According to the previous report, diffusion coefficient of Li^+ (D_{Li+}) can be estimated by the following equation [53].

$$D_{Li^+} = \frac{4L^2}{\pi\tau}\left(\frac{\Delta E_S}{\Delta E_\tau}\right)^2 \quad (1)$$

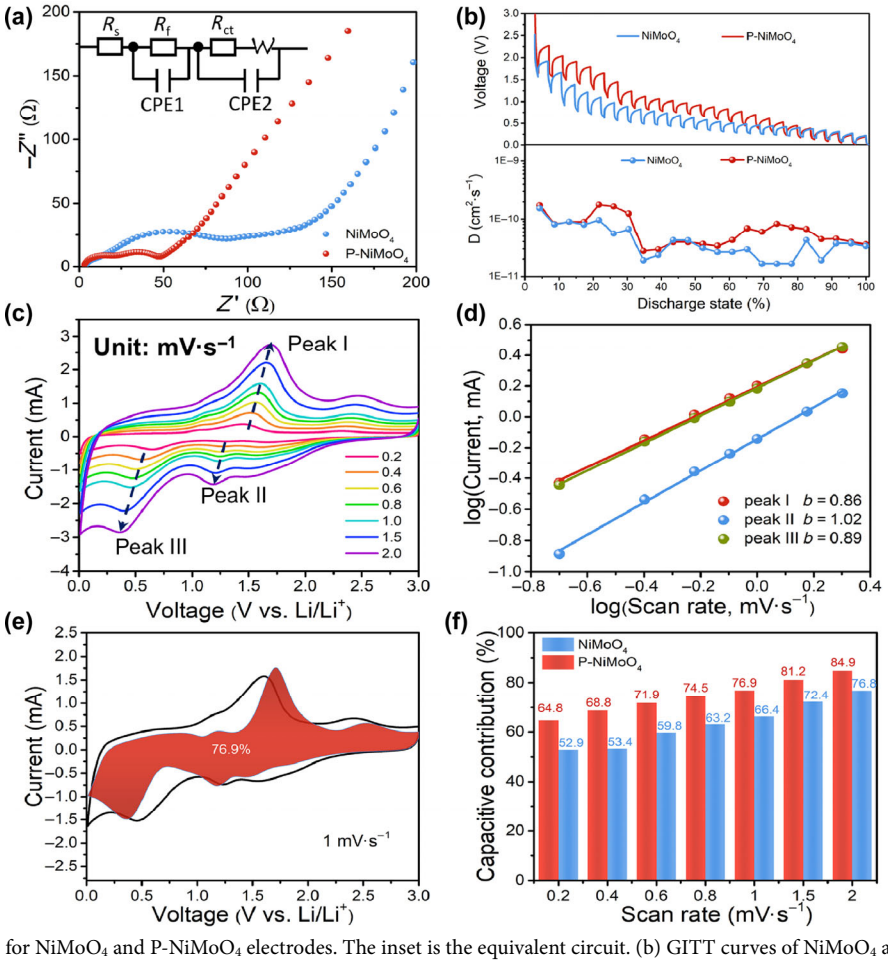

Figure 5 (a) EIS curves for $NiMoO_4$ and P-$NiMoO_4$ electrodes. The inset is the equivalent circuit. (b) GITT curves of $NiMoO_4$ and P-$NiMoO_4$ electrodes and the corresponding Li^+ diffusion coefficient at the first discharge process. (c) CV curves at different scan rates from 0.2 to 2.0 $mV·s^{-1}$, and (d) the corresponding log (*i*) versus log(*v*) plots at different redox peaks. (e) The proportion of capacitive-controlled contribution (the red area) of P-$NiMoO_4$ electrode at 1.0 $mV·s^{-1}$ and (f) the percentage of capacitive contribution of $NiMoO_4$ and P-$NiMoO_4$ electrodes at various sweep rates.

where τ (s) is the duration time of the pulse, L (cm) is Li^+ diffusion length (equal to the thickness of electrode for compact electrode), E_S (V) is the voltage change between steps, and ΔE_τ (V) is the voltage change during the pulse period. D_{Li+} values are calculated and plotted in light of various discharge depths. As presented in Fig. 5(b), P-$NiMoO_4$ electrode has a higher average diffusion coefficient compared with $NiMoO_4$ electrode, which can be attributed to the slightly enlarged interplanar spacing of P-$NiMoO_4$ observed from XRD patterns and HRTEM images. Such feature of P-$NiMoO_4$ nanorods is favorable for the diffusion of charge and thus enabling an impressive rate capability with regard to its use in LIBs.

To deeply investigate the electrochemical kinetics and outstanding rate capability of P-$NiMoO_4$ electrode, CV profiles at different scan rates (Fig. 5(c) and Fig. S8 in the ESM) were collected to recognize the capacity contribution during lithiation and delithiation processes. As one can see that all CV curves show the similar shapes, and the peak density enhances gradually along with the increase of sweep rate from the 0.2 to 2.0 $mV·s^{-1}$. The detailed relationship between peak density (*i*) and scan rate (*v*) is described as follows [54]

$$i = av^b \tag{2}$$

a and *b* are adjustable parameters. According to previous literature, the value of *b* presents the type of charge storage mechanism and can be obtained via plotting of log(*i*) and log(*v*). Specifically, *b* value near 1 implies a capacitance dominating during the electrochemical reaction process, while *b* approaching 0.5 demonstrate that the diffusion-controlled contribution is prevailing. As represented in Fig. 5(d), the calculated *b* value of anodic peak (peak I) and cathodic peaks (peak II and peak III) for P-$NiMoO_4$ electrode are 0.86, 1.02 and 0.89, respectively, which is slightly higher than that of $NiMoO_4$ electrode (Fig. S8 in the ESM). This result indicates that the redox kinetics process of P-$NiMoO_4$ electrode is controlled by a capacitance-controlled process, which can endow an impressive rate capability. Moreover, the detailed capacitive contribution can be quantitatively calculated using the following equation [55]

$$i = k_1 v + k_2 v^{\frac{1}{2}} \tag{3}$$

where k_1v and $k_2v^{1/2}$ indicate capacitive and diffusion-controlled contributions, respectively. As displayed in Fig. 5(e), the capacitive contribution of P-$NiMoO_4$ electrode is as high as 76.9% at 1 $mV·s^{-1}$ (represented by the red area), which is higher than that of $NiMoO_4$ electrode. Moreover, the proportion of capacitive contribution gradually evaluates with the increase in sweep rate, which can approach 89.3% at 2 $mV·s^{-1}$ (Fig. 5(f)). This suggests that P doping can enhance the capacitive-controlled contribution, which may originate from the one-dimensional nanorod structure with high surface-to-ratio and oxygen vacancies introduced by P doping. The BET specific surface of P-$NiMoO_4$ nanorods (36.9 $m^2·g^{-1}$) calculated from the nitrogen adsorption and desorption isotherms (Fig. S9 in the ESM) slightly higher than that of undoped $NiMoO_4$ (34.3 $m^2·g^{-1}$), which may ascribe to the phosphorization process. Another important reason is that the oxygen vacancies can provide more active sites on the surface of P-$NiMoO_4$ electrode, achieving

relatively high lithium storage capacity and outstanding rate capability of in LIBs.

To gain deep insight into the effect of P doping on the electronic structures of $NiMoO_4$, DFT calculations were performed based on the optimized geometrical structures of $NiMoO_4$ (220) as a model. Firstly, the substitution energy of oxygen is calculated based on the four different doping sites (Fig. S10 in the ESM). As shown in Fig. S11 in the ESM, the substitution energy of number 1, 2, 3 and 4 sites are −2.2, −0.14, −6.67 and −4.01 eV, respectively, which indicate that the phosphorus atoms preferentially substitute two sites (3 and 4). Meanwhile, the geometry of doped $NiMoO_4$ can be maintained without structure distortion. Subsequently, the band structures of $NiMoO_4$ and P-$NiMoO_4$ are firstly calculated based on the models of initial, signal P doping and diatomic P doping (Fig. S12 in the ESM). As depicted in Fig. 6(a), the bandgap of undoped $NiMoO_4$ is 0.71 eV at Y point, demonstrating a typical semiconductor property, and impeding the electronic transport from the circuit to the electrode surface. The bandgap of $NiMoO_4$ decreases from 0.71 to 0.55 eV for single P doing and further reduces to 0.36 eV for the diatomic P doing (Fig. 6(c) and Fig. S13(a) in the ESM). The above results demonstrate that the diatomic P doped $NiMoO_4$ exhibits smaller bandgap, indicating a significantly enhanced electronic conductivity after introducing two P into $NiMoO_4$. Furthermore, the density of states (DOS) of $NiMoO_4$ (Fig. 6(b)) and P-$NiMoO_4$ (Fig. 6(d) and Fig. S13(b) in the ESM) was also determined for the purpose of comparison. It is clearly observed that P-$NiMoO_4$ with diatomic P doping presents more occupations at Fermi level (obviously impure bands of P), from which a conclusion is deduced: new states produced by doping P around Fermi level can modify the electronic conductivity of bulk material with the decrease in the bandgap. This calculation result is also in good agreement with experimental results in the improvement of electronic conductivity for P-$NiMoO_4$ electrode, which could offer a powerful theoretical support for achieving high rate capacity in LIBs.

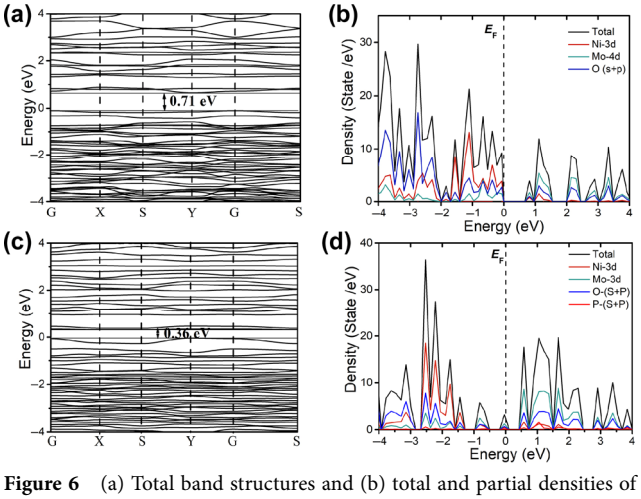

Figure 6 (a) Total band structures and (b) total and partial densities of states for $NiMoO_4$. (c) Total band structures and (d) total and partial densities of states diatomic P-$NiMoO_4$.

4 Conclusions

In summary, by focusing on the deficiency of $NiMoO_4$ as anode for LIBs, we designed heteroatom doping to enhance its intrinsic electronic conductivity for realizing an impressive rate performance. In this study, P-$NiMoO_4$ nanorods were fabricated by an untroublesome hydrothermal method followed by low-temperature phosphorization treatment. Based on the experimental results, P-$NiMoO_4$ electrode delivered a promising lithium storage capacity (1,130 mAh·g^{-1} at 100 mA·g^{-1} after 100 cycles), impressive rate performance (640 mAh·g^{-1} at 2,000 mA·g^{-1}), and excellent cycling stability (945 mAh·g^{-1} at 500 mA·g^{-1} over 200 cycles), which are superior to those of undoped $NiMoO_4$ electrode. The exceptional lithium storage performance is derived from the P doping, which can greatly heighten the electronic conductivity and generate some oxygen vacancies on the surface of $NiMoO_4$. DFT calculations further confirmed the enhanced electronic conductivity (narrowed bandgap) in P-$NiMoO_4$. Consequently, this work presents a feasible design and doping strategy to optimize the electronic conductivity of transition metal oxides by introducing nonmetal heteroatoms and achieves a high rate performance in LIBs.

Acknowledgements

This work was supported by the National Natural Science Foundation of China (Nos. 21878195 and U20A20145), the Scientific and technological achievement transformation project of Sichuan Science and Technology Department (No. 21ZHSF0111), and Shanghai Scientific and Technological Innovation Project (No. 18JC1410604).

Electronic Supplementary Material: Supplementary material (SAED images, XPS spectra, EPR spectra, nitrogen adsorption and desorption curves, CV and galvanostatic discharge-charge curves, SEM and EDX mapping images after long term cycling, DTF calculation models) is available in the online version of this article at https://doi.org/10.1007/s12274-021-3455-3.

References

[1] Reddy, M. V.; Rao, G. V. S.; Chowdari, B. V. R. Metal oxides and oxysalts as anode materials for Li ion batteries. *Chem. Rev.* **2013**, *113*, 5364–5457.

[2] Liu, Z. L.; Wang, X. X.; Wu, Z. Y.; Yang, S. J.; Yang, S. L.; Chen, S. P.; Wu, X. T.; Chang, X. H.; Yang, P. P.; Zheng, J. et al. Ultrafine Sn_4P_3 nanocrystals from chloride reduction on mechanically activated Na surface for sodium/lithium ion batteries. *Nano Res.* **2020**, *13*, 3157–3164.

[3] Fan, Z. Y.; Liang, J.; Yu, W.; Ding, S. J.; Cheng, S. D.; Yang, G.; Wang, Y. L.; Xi, Y. X.; Xi, K.; Kumar, R. V. Ultrathin NiO nanosheets anchored on a highly ordered nanostructured carbon as an enhanced anode material for lithium ion batteries. *Nano Energy* **2015**, *16*, 152–162.

[4] Sheng, Q. Q.; Li, Q.; Xiang, L. X.; Huang, T.; Mai, Y. Y.; Han, L. Double diamond structured bicontinuous mesoporous titania templated by a block copolymer for anode material of lithium-ion battery. *Nano Res.* **2021**, *14*, 992 – 997.

[5] Yue, H. L.; Wang, G. M.; Jin, R. C.; Wang, Q. Y.; Cui, Y. M.; Gao, S. M. Sulfur-doped amorphous $NiMoO_4$ on crystalline Fe_2O_3 nanorods for enhanced lithium storage performance. *J. Mater. Chem. A* **2018**, *6*, 23819–23827.

[6] Jiang, G. X.; Li, L.; Xie, Z. J.; Cao, B. Q. Facile fabrication of porous $NiMoO_4$@C nanowire as high performance anode material for lithium ion batteries. *Ceram. Int.* **2019**, *45*, 18462–18470.

[7] Park, J. S.; Cho, J. S.; Kang, Y. C. Scalable synthesis of $NiMoO_4$ microspheres with numerous empty nanovoids as an advanced anode material for Li-ion batteries. *J. Power Sources* **2018**, *379*, 278–287.

[8] Liu, W. L.; Zhi, H. Q.; Yu, X. B. Recent progress in phosphorus based anode materials for lithium/sodium ion batteries. *Energy Storage Mater.* **2019**, *16*, 290–322.

[9] Haetge, J.; Djerdj, I.; Brezesinski, T. Nanocrystalline $NiMoO_4$ with an ordered mesoporous morphology as potential material for rechargeable thin film lithium batteries. *Chem. Commun.* **2012**, *48*, 6726–6728.

[10] Wang, X.; Kim, H. M.; Xiao, Y.; Sun, Y. K. Nanostructured metal phosphide-based materials for electrochemical energy storage. *J. Mater. Chem. A* **2016**, *4*, 14915–14931.

[11] Huang, L.; Xiang, J. W.; Zhang, W.; Chen, C. J.; Xu, H. H.; Huang, Y. H.

3D interconnected porous $NiMoO_4$ nanoplate arrays on Ni foam as high-performance binder-free electrode for supercapacitors. *J. Mater. Chem. A* **2015**, *3*, 22081–22087.

[12] Wang, B.; Li, S. M.; Wu, X. Y.; Tian, W. M.; Liu, J. H.; Yu, M. Integration of network-like porous $NiMoO_4$ nanoarchitectures assembled with ultrathin mesoporous nanosheets on three-dimensional graphene foam for highly reversible lithium storage. *J. Mater. Chem. A* **2015**, *3*, 13691–13698.

[13] Xiao, K.; Xia, L.; Liu, G. X.; Wang, S. Q.; Ding, L. X.; Wang, H. H. Honeycomb-like $NiMoO_4$ ultrathin nanosheet arrays for high-performance electrochemical energy storage. *J. Mater. Chem. A* **2015**, *3*, 6128–6135.

[14] Wang, S. G.; Lin, J.; Fan, C. Y.; Li, Y. F.; Zhang, J. P.; Wu, X. L.; Sun, H. Z.; Deng, M. X.; Su, Z. M. Target encapsulating $NiMoO_4$ nanocrystals into 1D carbon nanofibers as free-standing anode material for lithium-ion batteries with enhanced cycle performance. *J. Alloys Compd.* **2020**, *830*, 154648.

[15] Perkins, J. D.; Paudel, T. R.; Zakutayev, A.; Ndione, P. F.; Parilla, P. A.; Young, D. L.; Lany, S.; Ginley, D. S.; Zunger, A.; Perry, N. H. et al. Inverse design approach to hole doping in ternary oxides: Enhancing *p*-type conductivity in cobalt oxide spinels. *Phys. Rev. B* **2011**, *84*, 205207.

[16] Zou, X. X.; Su, J. A.; Silva, R.; Goswami, A.; Sathe, B. R.; Asefa, T. Efficient oxygen evolution reaction catalyzed by low-density Ni-doped Co_3O_4 nanomaterials derived from metal-embedded graphitic C_3N_4. *Chem. Commun.* **2013**, *49*, 7522–7524.

[17] Song, H.; Yun, S. W.; Chun, H. H.; Kim, M. G.; Chung, K. Y.; Kim, H. S.; Cho, B. W.; Kim, Y. T. Anomalous decrease in structural disorder due to charge redistribution in Cr-doped $Li_4Ti_5O_{12}$ negative-electrode materials for high-rate Li-ion batteries. *Energy Environ. Sci.* **2012**, *5*, 9903–9913.

[18] Banerjee, S.; Debata, S.; Madhuri, R.; Sharma, P. K. Electrocatalytic behavior of transition metal (Ni, Fe, Cr) doped metal oxide nanocomposites for oxygen evolution reaction. *Appl. Surf. Sci.* **2018**, *449*, 660–668.

[19] Chen, C. C.; Huang, Y. A.; Zhang, H.; Wang, X. F.; Wang, Y. J.; Jiao, L. F.; Yuan, H. T. Controllable synthesis of Cu-doped CoO hierarchical structure for high performance lithium-ion battery. *J. Power Sources* **2016**, *314*, 66–75.

[20] Yan, C. S.; Zhu, Y.; Li, Y. T.; Fang, Z. W.; Peng, L. L.; Zhou, X.; Chen, G.; Yu, G. H. Local built-in electric field enabled in carbon-doped Co_3O_4 nanocrystals for superior lithium-ion storage. *Adv. Funct. Mater.* **2018**, *28*, 1705951.

[21] Yan, C. S.; Chen, G.; Zhou, X.; Sun, J. X.; Lv, C. D. Template-based engineering of carbon-doped Co_3O_4 hollow nanofibers as anode materials for lithium-ion batteries. *Adv. Funct. Mater.* **2016**, *26*, 1428–1436.

[22] Song, H.; Kim, Y. T. A Mo-doped $TiNb_2O_7$ anode for lithium-ion batteries with high rate capability due to charge redistribution. *Chem. Commun.* **2015**, *51*, 9849–9852.

[23] Guan, B. Y.; Yu, L.; Lou, X. W. General synthesis of multishell mixed-metal oxyphosphide particles with enhanced electrocatalytic activity in the oxygen evolution reaction. *Angew. Chem., Int. Ed.* **2017**, *56*, 2386–2389.

[24] Xiao, Z. H.; Wang, Y.; Huang, Y. C.; Wei, Z. X.; Dong, C. L.; Ma, J. M.; Shen, S. H.; Li, Y. F.; Wang, S. Y. Filling the oxygen vacancies in Co_3O_4 with phosphorus: An ultra-efficient electrocatalyst for overall water splitting. *Energy Environ. Sci.* **2017**, *10*, 2563–2569.

[25] Kresse, G; Furthmuller, J. Efficiency of ab-initio total energy calculations for metals and semiconductors using a plane-wave basis set. *Comput. Mater. Sci.* **1999**, *6*, 15–50.

[26] Segall, M. D.; Lindan, P. J. D.; Probert, M. J.; Pickard, C. J.; Hasnip, P. J.; Clark, S. J.; Payne, M. C. First-principles simulation: Ideas, illustrations and the CASTEP code. *J. Phys.: Condens. Matter* **2002**, *14*, 2717–2744.

[27] Blöchl, P. E. Projector augmented-wave method. *Phys. Rev. B, Condens. Matter* **1994**, *50*, 17953–17979.

[28] Perdew, J. P.; Burke, K.; Ernzerhof, M. Generalized gradient approximation made simple. *Phys. Rev. Lett.* **1996**, *77*, 3865–3868.

[29] Grimme, S. Semiempirical GGA-type density functional constructed with a long-range dispersion correction. *J. Comput. Chem.* **2006**, *27*, 1787–1799.

[30] Asahi, R.; Morikawa, T.; Irie, H.; Ohwaki, T. Nitrogen-doped titanium dioxide as visible-light-sensitive photocatalyst: Designs, developments, and prospects. *Chem. Rev.* **2014**, *114*, 9824–9852.

[31] Yue, L. C.; Zhao, H. T.; Wu, Z. G.; Liang, J.; Lu, S. Y.; Chen, G.; Gao, S. Y.; Zhong, B. H.; Guo, X. D.; Sun, X. P. Recent advances in electrospun one-dimensional carbon nanofiber structures/heterostructures as anode materials for sodium ion batteries. *J. Mater. Chem. A* **2020**, *8*, 11493–11510.

[32] Wang, H. G.; Yuan, S.; Ma, D. L.; Zhang, X. B.; Yan, J. M. Electrospun materials for lithium and sodium rechargeable batteries: From structure evolution to electrochemical performance. *Energy Environ. Sci.* **2015**, *8*, 1660–1681.

[33] Yue, H. L.; Wang, G. M.; Xu, Y. K.; Jin, R. C.; Wang, Q. Y.; Gao, S. M. Oxygen-deficient $NiMoO_{4-x}S_x$ nanosheets perpendicularly grown on N-doped carbon nanosheets for high performance lithium-ion batteries. *J. Power Sources* **2020**, *455*, 227947.

[34] Wang, Y.; Pan, Q.; Jia, K.; Wang, H. B.; Gao, J. J.; Xu, C. L.; Zhong, Y. J.; Alshehri, A. A.; Alzahrani, K. A.; Guo, X. D. et al. Ni_2P nanosheets on carbon cloth: An efficient flexible electrode for sodium-ion batteries. *Inorg. Chem.* **2019**, *58*, 6579–6583.

[35] An, L.; Feng, J. R.; Zhang, Y.; Wang, R.; Liu, H. W.; Wang, G. C.; Cheng, F. Y.; Xi, P. X. Epitaxial heterogeneous interfaces on N-$NiMoO_4$/NiS_2 nanowires/nanosheets to boost hydrogen and oxygen production for overall water splitting. *Adv. Funct. Mater.* **2019**, *29*, 1805298.

[36] Ghosh, D.; Giri, S.; Das, C. K. Synthesis, characterization and electrochemical performance of graphene decorated with 1D $NiMoO_4{\cdot}nH_2O$ nanorods. *Nanoscale* **2013**, *5*, 10428–10437.

[37] Xing, Z.; Kong, W. H.; Wu, T. W.; Xie, H. T.; Wang, T.; Luo, Y. L.; Shi, X. F.; Asiri, A. M.; Zhang, Y. N.; Sun, X. P. Hollow Bi_2MoO_6 sphere effectively catalyzes the ambient electroreduction of N_2 to NH_3. *ACS Sustainable Chem. Eng.* **2019**, *7*, 12692–12696.

[38] Zhao, D.; Qin, J. W.; Zheng, L. R.; Cao, M. H. Amorphous vanadium oxide/molybdenum oxide hybrid with three-dimensional ordered hierarchically porous structure as a high-performance Li-ion battery anode. *Chem. Mater.* **2016**, *28*, 4180–4190.

[39] Wang, Z. C.; Liu, H. L.; Ge, R. X.; Ren, X.; Ren, J.; Yang, D. J.; Zhang, L. X.; Sun, X. P. Phosphorus-doped Co_3O_4 nanowire array: A highly efficient bifunctional electrocatalyst for overall water splitting. *ACS Catal.* **2018**, *8*, 2236–2241.

[40] Pan, Q.; Chen, H.; Wu, Z. G.; Wang, Y.; Zhong, B. H.; Xia, L.; Wang, H. Y.; Cui, G. W.; Guo, X. D.; Sun, X. P. Nanowire of WP as a high-performance anode material for sodium - ion batteries. *Chem.–Eur. J.* **2019**, *25*, 971–975.

[41] Wang, Q.; He, H. N.; Luan, J. Y.; Tang, Y. G.; Huang, D.; Peng, Z. G.; Wang, H. Y. Synergistic effect of N-doping and rich oxygen vacancies induced by nitrogen plasma endows TiO_2 superior sodium storage performance. *Electrochim. Acta* **2019**, *309*, 242–252.

[42] Zhang, Y. H.; Dai, R. Y.; Hu, S. R. Study of the role of oxygen vacancies as active sites in reduced graphene oxide-modified TiO_2. *Phys. Chem. Chem. Phys.* **2017**, *19*, 7307–7315.

[43] Wang, B. B.; Wang, G.; Cheng, X. M.; Wang, H. Synthesis and electrochemical investigation of core-shell ultrathin NiO nanosheets grown on hollow carbon microspheres composite for high performance lithium and sodium ion batteries. *Chem. Eng. J.* **2016**, *306*, 1193–1202.

[44] Sun, Y. X.; Wang, J.; Zhao, B. T.; Cai, R.; Ran, R.; Shao, Z. P. Binder-free α-MoO_3 nanobelt electrode for lithium-ion batteries utilizing van der Waals forces for film formation and connection with current collector. *J. Mater. Chem. A* **2013**, *1*, 4736–4746.

[45] Liu, S. D.; Lee, S. C.; Patil, U. M.; Ray, C.; Sankar, K. V.; Zhang, K.; Kundu, A.; Kang, S.; Park, J. H.; Jun, S. C. Controllable sulfuration engineered NiO nanosheets with enhanced capacitance for high rate supercapacitors. *J. Mater. Chem. A* **2017**, *5*, 4543–4549.

[46] Meduri, P.; Clark, E.; Kim, J. H.; Dayalan, E.; Sumanasekera, G. U.; Sunkara, M. K. MoO_{3-x} nanowire arrays as stable and high-capacity anodes for lithium ion batteries. *Nano Lett.* **2012**, *12*, 1784–1788.

[47] Cho, J. S.; Lee, S. Y.; Ju, H. S.; Kang, Y. C. Synthesis of NiO nanofibers composed of hollow nanospheres with controlled sizes by the nanoscale kirkendall diffusion process and their electrochemical properties. *ACS Appl. Mater. Interfaces* **2015**, *7*, 25641–25647.

[48] Wu, J.; Yin, W. J.; Liu, W. W.; Guo, P.; Liu, G. B.; Liu, X. C.; Geng, D.

S.; Lau, W. M.; Liu, H.; Liu, L. M. High performance NiO nanosheets anchored on three-dimensional nitrogen-doped carbon nanotubes as a binder-free anode for lithium ion batteries. *J. Mater. Chem. A* **2016**, *4*, 10940–10947.

[49] Ni, J. F.; Fu, S. D.; Wu, C.; Maier, J.; Yu, Y.; Li, L. Self-supported nanotube arrays of sulfur-doped TiO_2 enabling ultrastable and robust sodium storage. *Adv. Mater.* **2016**, *28*, 2259–2265.

[50] Yang, F. H.; Gao, H.; Hao, J. N.; Zhang, S. L.; Li, P.; Liu, Y. Q.; Chen, J.; Guo, Z. P. Yolk-shell structured FeP@C nanoboxes as advanced anode materials for rechargeable lithium-/potassium-ion batteries. *Adv. Funct. Mater.* **2019**, *29*, 1808291.

[51] Zhang, J.; Chen, Y. L.; Chu, R. X.; Jiang, H.; Zeng, Y. B.; Zhang, Y.; Huang, N. M.; Guo, H. Pseudocapacitive P-doped $NiCo_2O_4$ microspheres as stable anode for lithium ion batteries. *J. Alloys Compd.* **2019**, *787*, 1051–1062.

[52] Wang, Y.; Wu, C. J.; Wu, Z. G.; Cui, G. W.; Xie, F. Y.; Guo, X. D.; Sun, X. P. FeP nanorod arrays on carbon cloth: A high-performance anode for sodium-ion batteries. *Chem. Commun.* **2018**, *54*, 9341–9344.

[53] Cao, D. W.; Kang, W. P.; Wang, W. H.; Sun, K. A.; Wang, Y. Y.; Ma, P.; Sun, D. F. Okra-like Fe_7S_8/C@ZnS/N-C@C with core-double-shelled structures as robust and high-rate sodium anode. *Small* **2020**, *16*, 1907641.

[54] Liu, P.; Han, J.; Zhu, K. J.; Dong, Z. H.; Jiao, L. F. Heterostructure $SnSe_2$/ZnSe@PDA nanobox for stable and highly efficient sodium-ion storage. *Adv. Energy Mater.* **2020**, *10*, 2000741.

[55] Zheng, Z. M.; Wu, H. H.; Liu, H. D.; Zhang, Q. B.; He, X.; Yu, S. C.; Petrova, V.; Feng, J.; Kostecki, R.; Liu, P. et al. Achieving fast and durable lithium storage through amorphous FeP nanoparticles encapsulated in ultrathin 3D P-doped porous carbon nanosheets. *ACS Nano* **2020**, *14*, 9545–9561.